Polar-direct-drive experiments with contoured-shell targets on OMEGA

F. J. Marshall, P. B. Radha, M. J. Bonino, J. A. Delettrez, R. Epstein, V. Yu. Glebov, D. R. Harding, C. Stoeckl, J. A. Frenje, M. Gatu Johnson, F. H. Séguin, H. Sio, A. Zylstra, and E. Giraldez

Citation: Physics of Plasmas **23**, 012711 (2016); doi: 10.1063/1.4940939
View online: http://dx.doi.org/10.1063/1.4940939
View Table of Contents: http://scitation.aip.org/content/aip/journal/pop/23/1?ver=pdfcov
Published by the AIP Publishing

Polar-direct-drive experiments with contoured-shell targets on OMEGA

F. J. Marshall,[1] P. B. Radha,[1] M. J. Bonino,[1] J. A. Delettrez,[1] R. Epstein,[1] V. Yu. Glebov,[1] D. R. Harding,[1] C. Stoeckl,[1] J. A. Frenje,[2] M. Gatu Johnson,[2] F. H. Séguin,[2] H. Sio,[2] A. Zylstra,[2] and E. Giraldez[3]
[1]*Laboratory for Laser Energetics, University of Rochester, 250 East River Road, Rochester, New York 14623-1299, USA*
[2]*Plasma Science and Fusion Center, Massachusetts Institute of Technology, Cambridge, Massachusetts 02139, USA*
[3]*General Atomics, San Diego, California 92121, USA*

(Received 30 October 2015; accepted 14 January 2016; published online 28 January 2016)

Polar-driven direct-drive experiments recently performed on the OMEGA Laser System have demonstrated the efficacy of using a target with a contoured shell with varying thickness to improve the symmetry and fusion performance of the implosion. The polar-driven contoured-shell implosions have substantially reduced low mode perturbations compared to polar-driven spherical-shell implosions as diagnosed by x-ray radiographs up to shell stagnation. Fusion yields were increased by more than a factor of ~2 without increasing the energy of the laser by the use of contoured shells. © *2016 AIP Publishing LLC*. [http://dx.doi.org/10.1063/1.4940939]

I. INTRODUCTION

The polar-direct-drive (PDD) approach to inertial confinement fusion[1] is being pursued as a means of demonstrating thermonuclear ignition at the National Ignition Facility[2] (NIF) with the beams of the NIF in the indirect-drive configuration. Extensive experiments have been performed on the OMEGA Laser System[3] to evaluate this technique.[4–9] Ignition target designs using cryogenically cooled, DT-filled CH shells have been investigated using two-dimensional (2-D) hydrodynamic simulations.[10,11] These simulations suggest that gains of at least 20 to 30 can be achieved using 1.5 MJ of laser energy to irradiate a DT-ice-layer–bearing cryogenic target. In the simulation study by Collins *et al.*,[11] the drive symmetry was optimized by using a combination of beam pointing, beam shaping, pulse shaping, and cryogenic fuel-layer shaping. The ideal ice layer is thinner at the target equator, where the beam illumination is the most oblique, and energy coupling to the target is reduced. The inclusion of an ice-layer-thickness variation increased the gain of the ignited plasma in this simulation. Collins *et al.* also noted that a thickness variation applied to the CH capsule could equivalently be used to shape the imploding plasma.

Since the Collins *et al.* study, experiments have been performed on both OMEGA[9] and the NIF,[12,13] making it clear that the laser–plasma interaction (LPI) loss mechanism referred to as cross-beam energy transfer[14] (CBET) plays an important role in the low-mode shape of PDD implosions. The magnitude of the CBET effect[15] is expected to be greater at higher intensities and longer LPI scale lengths, such as those that exist in experiments on the NIF. While experiments performed on OMEGA at intensities of $\sim 6 \times 10^{14}$ W/cm^2 (Ref. 9) showed good agreement between experiments and simulation, without consideration of the effect of CBET on the equatorial drive, those performed on the NIF at much higher intensities[13] (ranging from 1 to 2×10^{15} W/cm^2), and assumed-to-be larger LPI scale lengths, showed a marked change in the low-mode implosion symmetry. Murphy *et al.*[13] show that when equatorial beams are assumed to be reduced in their coupling by a mechanism such as CBET, then the simulations more closely match the experiments. Hohenberger *et al.*[12] have performed PDD experiments on the NIF at an intensity of $\sim 1 \times 10^{15}$ W/cm^2 and found an improved agreement between the measured and simulated shell trajectory, and the measured and simulated low-mode shapes, when the effect of CBET is included in the simulations.

This article presents results of polar-driven implosions (40 beams) using shells with a contoured thickness (thickness varying with angle from the polar-drive axis), demonstrating that improved implosion symmetry and fusion performance are obtained relative to polar-driven spherical shells. Comparison implosions were performed with symmetrically driven (60 beams) spherical shells using an equal energy on target (i.e., single-beam energy reduced to ~2/3 of the 40-beam implosions). The yields of the polar-driven contoured shells approach those of the symmetrically driven spherical shells, nearly removing the performance penalty incurred by polar drive. These experiments were performed at an intensity of $\sim 4 \times 10^{14}$ W/cm^2, where CBET is expected to be of minimal contribution. In a complementary set of experiments, Séguin *et al.*[16] have demonstrated the ability to introduce a controlled asymmetry to implosions by using symmetrically driven contoured shells.

II. CONTOURED SHELLS

The unablated shell material in a laser-driven implosion behaves much like the payload of a rocket.[17] The final velocity of the unablated shell depends nonlinearly on the initial shell thickness and the intensity of the laser light being used to accelerate the shell through ablation.[17] For PDD, the intensity varies as a function of both polar angle and time.

Optimizing PDD is accomplished by picking the beam shapes, beam pointing, pulse shapes, and target profile that result in the most spherically shaped implosion, leading to the highest target gain. This is done experimentally and with simulations using a 2-D hydrodynamics code. If it is assumed that lateral mass flow in the imploding shell can be neglected, then the simulations can be performed with a 1-D hydrocode, provided that the amount of absorbed energy can be accurately predicted. To apply this to PDD, it is assumed that the average absorbed intensity is solely a function of polar angle. The capsule thickness as a function of polar angle needed to compensate for the angular variation of the average intensity can therefore be determined from a series of 1-D simulations. This is illustrated in Fig. 1, where the calculated trajectories of the fuel–shell interface R_{fs} as a function of time for two D_2-filled CH shells with identical inner shell radii (412 μm) and fill pressure (10 atm), but with differing shell thicknesses of 24 and 27 μm, respectively, are shown. The simulations were performed with the 1-D hydrocode *LILAC*[18] for nominal laser conditions of 27 kJ of UV light in a 1-ns square pulse ($\sim 1 \times 10^{15}$ W/cm^2 at a radius of 430 μm). The 27-μm shell implodes more slowly than the 24-μm shell. R_{fs} is also shown for an intensity reduced to 80% of the nominal case. This trajectory (dashed line) is nearly identical to that of the 27-μm-thick shell at the nominal intensity. Note that for these simulations, absorption of the UV laser beams was assumed to be solely by the inverse bremsstrahlung effect and so does not include the effect of CBET, which can reduce the amount of energy absorbed in the plasma and for PDD has the largest effect on the equatorial drive. The magnitude of the CBET effect is expected to be greater at higher intensities,[15] so this trajectory prediction as a function of intensity may benefit from its inclusion but is otherwise outside the scope of this work.

With these provisos, a series of such simulations were performed to determine the approximate shell thickness as a function of average intensity needed so that R_{fs} was the same as the nominal intensity case at a time close to shell stagnation. Figure 2 shows values of R_{fs} at $t = 2.0$ ns, when the fuel–shell interface is close to a minimum, for shell

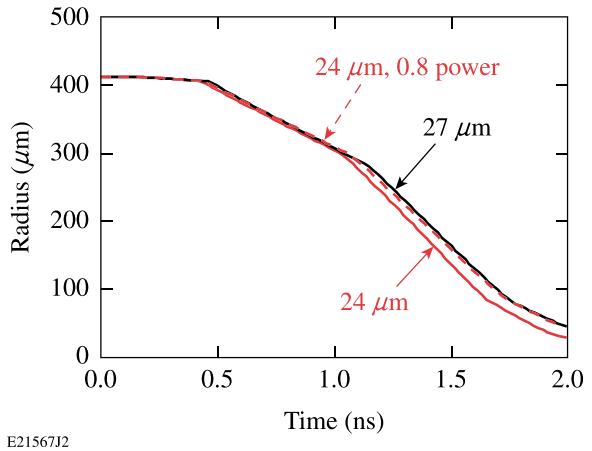

FIG. 1. Simulated fuel–shell interface R_{fs} trajectory for a 24- and a 27-μm-thick shell at nominal laser conditions (27 kJ, 1-ns square pulse), and for a 24-μm-thick shell at 0.8× nominal laser intensity.

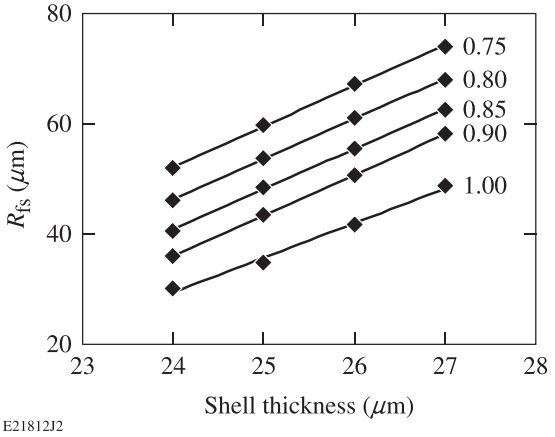

FIG. 2. Simulated values of R_{fs} at $t = 2.0$ ns as a function of shell thickness for cases of 0.75, 0.8, 0.85, 0.9, and 1.0× nominal laser intensity.

thicknesses Δr from 24 to 27 μm and intensities I of 0.75 to 1.0× nominal. A straight line was fit to each set of values of R_{fs} for a given I. The value of shell thickness Δr as a function of intensity that results in an R_{fs} of 49 μm at $t = 2.0$ ns was determined from these fits by linear regression. The resulting equation for Δr in microns as a function of intensity is given by

$$\Delta r = 6.4 + 29.6I - 9.0I^2, \tag{1}$$

where I is in units of the nominal intensity. The lowest even-mode intensity perturbation that could result from PDD illumination is the second Legendre mode, i.e., $\mathscr{L} = 2$. By restricting the perturbation to this first even Legendre mode, the intensity is given by

$$I(\theta) = I_0\left[1 + \frac{i_2}{2}(3\cos^2\theta - 1)\right]\Big/(1 + i_2), \tag{2}$$

where I_0 is the intensity at $\theta = 0$ and i_2 is the amplitude of the $\mathscr{L} = 2$ mode. When Eq. (2) is substituted into Eq. (1), the ideal shell thickness profile is determined for this intensity profile.

The contoured shells used in these experiments were manufactured by precision machining at the General Atomics (GA) Target Facility.[19] The profile was chosen by assuming that the average $i_2 = +0.1$ in Eq. (2) above. This choice corresponds to a 10% prolate intensity profile and results in a shell thinner at the equator to compensate for the reduced drive at the equator. To accomplish this process on a lathe using a single mounting direction, it was decided to avoid machining the shells near the poles (also the rotation axis of the lathe), avoiding errors in alignment introduced by switching the mounting direction of the target from one pole to the other. This leaves a region of constant shell thickness near the poles. Figure 3 shows the ideal profile (a modified profile that avoids the need to machine the poles) and an actual measured profile for one GA-machined shell. The modified profile is arrived at from the ideal profile by setting Δr equal to a constant from 0° to 30° and then using $\Delta r = \Delta r(\theta')$, where $\theta' = (\theta - 30°) \times 1.5$ for $30° \le \theta \le 90°$. Both profiles were adjusted by a constant to match the actual

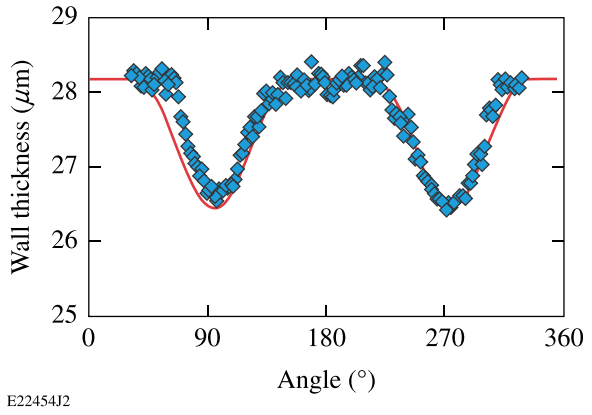

FIG. 3. Measured contoured-shell thickness as a function of polar angle compared to the ideal profile and modified profile that avoids the need to machine near the poles.

shell thickness at the poles. The shell thickness of the contoured shells, as a function of angle from the machining pole, was determined by x-ray radiography. Departures from the desired modified profile are seen to be ~0.1 μm for the example shell thickness profile shown in Fig. 3. Four such targets were used in OMEGA experiments and the results are compared to targets that were manufactured in an identical fashion at GA but did not undergo machining.

III. EXPERIMENTS

Experiments were performed on OMEGA in the PDD configuration, where 40 of the 60 OMEGA beams are used to illuminate the target[5] (Fig. 4), and comparison implosions were performed in 60-beam symmetric mode, where all beams are aimed at the center of the target. For the 60-beam, symmetrically driven implosions the energy per beam was reduced to 2/3 of that for the 40-beam, polar-driven implosions, keeping the total energy approximately the same. All targets were 10-atm D_2 gas filled by diffusion through a

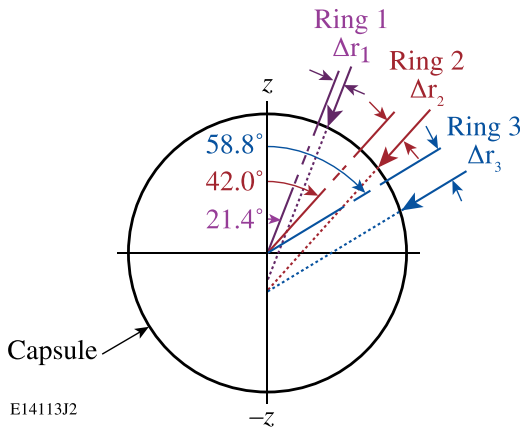

FIG. 4. Schematic of the beam-pointing offsets used in this work. For polar drive, all beams in a given ring are re-aimed toward the equator by an amount Δr, which can be different for each ring. There are five beams in rings 1 and 2, and ten beams in ring 3. Not shown are the three rings in the bottom half of the sphere with the same number of beams per ring which make the same angles from the $-z$ axis. Symmetric drive is with 20 additional beams, 10 at an angle of 81.25° from the $+z$ axis, ten at the same angle from the $-z$ axis, and all Δr's are zero.

0.1-μm-thick Al gas retention layer. The experiments were performed with ~14 kJ ($E_{ave} = 13.8$ kJ, with a range from 13.0 to 15.0 kJ, i.e., ±7%) of UV light (351 nm) using a ~3-ns-duration, triple-picket pulse shape[7] designed to keep the target on a low adiabat, obtaining a high convergence ratio (CR, the ratio of the initial fuel-shell radius to the final fuel-shell radius). CRs of ~19 were calculated for these experiments. The OMEGA laser beams were smoothed using 0.5-THz bandwidth, smoothing by spectral dispersion (SSD)[20] with polarization smoothing.[21] The beam profiles were shaped using distributed phase plates (DPPs), resulting in a super-Gaussian beam shape given by $I/I_0 = \exp[-(r/r_0)^n]$ with $r_0 = 308\ \mu$m and $n = 3.66$.[22] These are designated as SG4 DPPs. The on-target intensity, averaged over polar angle and at the peak of the main pulse, was $\sim 4 \times 10^{14}$ W/cm^2 (defined at the initial target radius).

The contoured shells were not built specifically with polar drive in mind, but with the expectation that PDD implosion symmetry could be improved if less laser light has to be directed to the target equator to compensate for the lower relative absorbed energy. It follows that the optimum choice of beam pointing to take advantage of a contoured shell should result in smaller beam offsets than for a spherical shell. Such an "optimum beam-pointing choice" was arrived at by using the modified capsule thickness profile as input to a series of *DRACO* 2-D hydrocode simulations[23] with varying beam pointing. Again the simulations assumed that absorption was solely by the inverse bremsstrahlung effect. Beam offset is used to quantify beam pointing, with the magnitude being the distance from beam center to target center, perpendicular to the beam propagation direction and with a positive offset meaning toward the equator of the PDD axis[5] (Fig. 4). All beams are re-aimed toward the target equator, with no change in the azimuthal beam pointing. A beam pointing of 0-, 120-, and 140-μm offsets for rings 1, 2, and 3, respectively, was found to produce the most-symmetric implosions for the nominal laser conditions given above and for the nominal modified shell thickness as described above. The beam pointing for rings 1, 2, and 3 are therefore referred to as "beam-pointing case (a, b, c)" where a, b, and c are the ring offsets in microns. This beam-pointing case (0, 120, 140) has offsets that are in fact less than that previously found to minimize the $\mathscr{L} = 2$ mode for spherically symmetric shells with PDD described in Marshall *et al.*[6] [beam-pointing case (90, 150, 150)]. The OMEGA beams were precision pointed to an accuracy of ~8 μm (rms) to these ideal offset locations using the method described in Ref. 22. This precision pointing method was applied to all choices of beam pointing used in this work, including 60-beam symmetric drive.

The time-dependent shapes of the polar-driven imploding shells were measured with framed x-ray backlighting, using a 6-μm-thick Ti foil illuminated by 8 of the 20 remaining OMEGA beams. The beams were overlapped onto the foil, four on each side, and defocused to a diameter of 0.7 mm. The foil was thin enough (6 μm) to be nearly transparent to the principal Ti-emitting line at 4.75 keV (Heα), effectively doubling the backlighter brightness. The backlighter was placed on the opposite side of the target from a

high-speed framing camera[24] having four strips, each timed to capture an array of images from 10-μm-diam pinholes with a magnification of 6 and spaced so that the separation in time of each image was 30 ps. The view of the target was 11° from the equator of the PDD axis, where the shapes of the observed radiographs were almost the same as at the equator (within ~2% for pure $\mathscr{L}$ modes at this angle, see Ref. 5). Absolute frame times were determined from observations of the backlighter onset on the first strip, from the measured strip-to-strip delay, and from the image-to-image time delay on a strip. An absolute time accuracy of ~50 ps was obtained with a frame-to-frame time accuracy of ~15 ps. The recorded images were corrected for film sensitivity as described in Ref. 6.

Figure 5 shows sample intensity-corrected images containing absorption by the unablated, imploding cold CH plasma of a polar-driven spherical shell and a polar-driven contoured shell implosion. Times are from the end of the laser pulse (~3.0 ns) until shell stagnation (~3.6 ns). Core self-emission is seen in the latest time frames for each. As can be seen from the images, the contoured shells implode with a more spherical shape for this beam pointing and the core self-emission also shows improved symmetry. Note also that the frame times for both Fig. 5(c) (spherical shell) and Fig. 5(g) (contoured shell) are the same, meaning core stagnation time is approximately the same for both within the uncertainty of the frame time (~50 ps). The equator of the contoured shell traveled farther, making the core more symmetric (see also the fusion neutron-production rates later in this section).

The shapes of the imploding plasmas are quantified by fitting the positions of the observed peak absorption as a function of angle to the PDD axis. In the case of an ideal optically thin, thin-shell absorber, the peak absorption corresponds to the inner radius of the shell. Therefore, the fuel–shell interface radius is approximately determined as a function of angle around the shell by measuring this peak absorption position. The most-probable values of the peak absorption positions are taken as the centroid of values above 80% of the maximum absorption observed in that direction. With the peak positions so determined, the center is determined by iteration, choosing the position that minimizes the difference between the left and right side of the radiograph, and likewise for top and bottom. Figure 6 shows sample fits to both measured and simulated radiographs for a polar-driven spherical shell and the same comparison is shown in Fig. 7 for a polar-driven contoured shell. The simulated radiographs are determined from *DRACO* simulations. The shell shape is included in the contoured-shell target simulations by a Legendre-mode decomposition up to mode 10 of the measured shell thickness of the contoured-shell target as a function of angle to the PDD axis. The simulations were post-processed by the code *Spect3D*,[25] which takes into account radiation transport, spatial blurring (~15 μm), and integration over the frame time (30 ps). The simulations are compared to the experimental results by fitting the peaks of the simulated absorption as a function of angle as is done for the measured radiographs. The comparisons with the *DRACO* simulations are at the time in the simulation when the fit to the simulation is at the same average radius as in the experiment.

Figures 8 and 9 show comparisons of the measured and simulated peak absorption positions as a function of angle from the polar drive axis for the radiographs shown in Figs. 6 and 7. In these comparisons, positive angles are clockwise from the top (right side of the radiograph) and negative angles correspond to the left side of the radiograph. Values shown are fractional deviations from the mean radius for that time. The spherical shell shows a pronounced peak near the equator that grows in time to ~20% greater than the average radius. The simulation closely matches the observed oblate perturbation. The perturbation of the contoured shell is much lower (≲5% for all times shown). A predicted small perturbation at the equator is not seen in the experiment.

Figures 10 and 11 show Legendre mode fits (up to order 10) of the two latest times for both the spherical and contoured shell radiograph peaks [Figs. 8(c) and 9(c)]. The

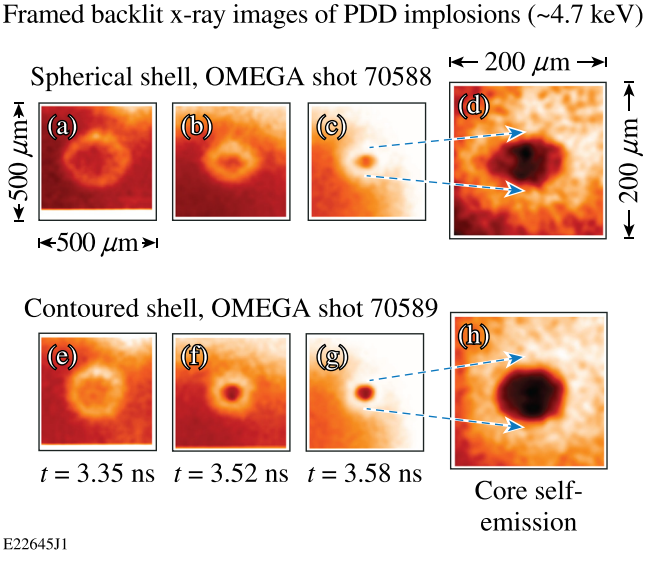

FIG. 5. Sample radiographs of 500 × 500-μm regions centered on the imploding plasma shell for [(a)–(c)] a polar-driven spherical shell and [(e)–(g)] a polar-driven contoured shell. Expanded regions showing the stagnation region self-emission are also shown for the (d) spherical shell and (h) contoured shell.

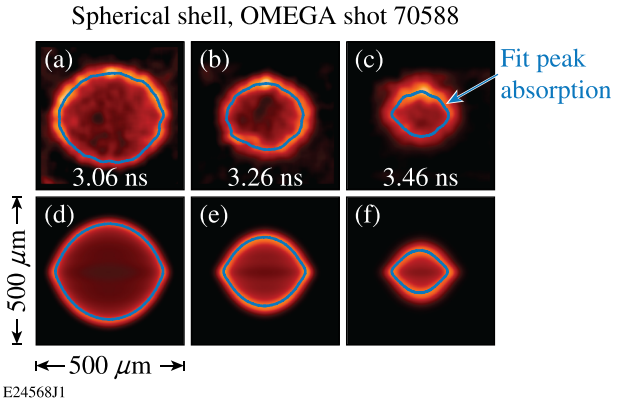

FIG. 6. (a)–(c) Fits to radiographs of a polar-driven spherical-shell implosion and (d)–(f) fits to simulated radiographs at the same average radii.

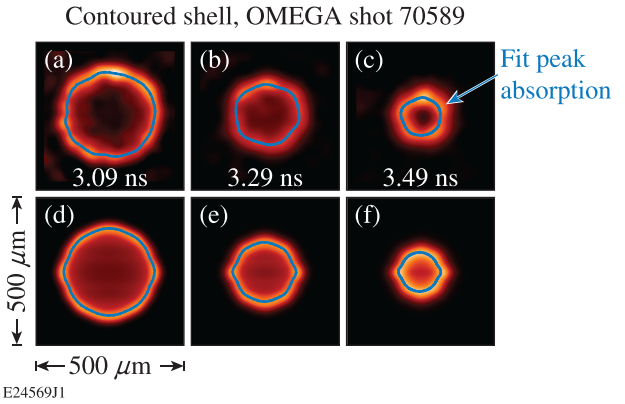

FIG. 7. (a)–(c) Fits to radiographs of a polar-driven contoured-shell implosion and (d)–(f) fits to simulated radiographs at the same average radii.

values shown are normalized to the average radius. In both cases, the right side and left side of the images are fit separately. The values shown are the left/right averages with the errors taken as the difference. For the spherical shell (Fig. 10), the simulation closely matches the measured radiograph $\mathscr{L}$-mode spectrum in sign and magnitude. For the contoured shell (Fig. 11), the magnitudes of the measured $\mathscr{L}$ modes are significantly reduced. While the simulation predicts lower $\mathscr{L}$-mode amplitudes, there is no longer a precise match of the values. Nevertheless, a large reduction of the shell perturbation is both observed and predicted by simulation. The net effect of the contoured shell is to increase the convergence ratio of the shell at the equator and therefore increase the compression of the contained fuel.

Mode amplitudes (normalized to the average radius) of the fits at all measured CRs for the two most-significant

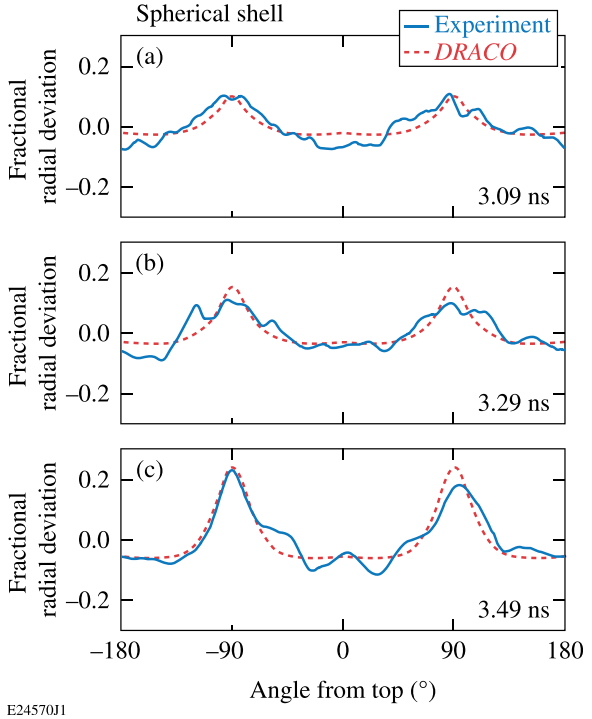

FIG. 8. Comparison of radiograph peak absorption shape with *DRACO* simulated shapes for the polar-driven spherical shell implosion shown in Fig. 5.

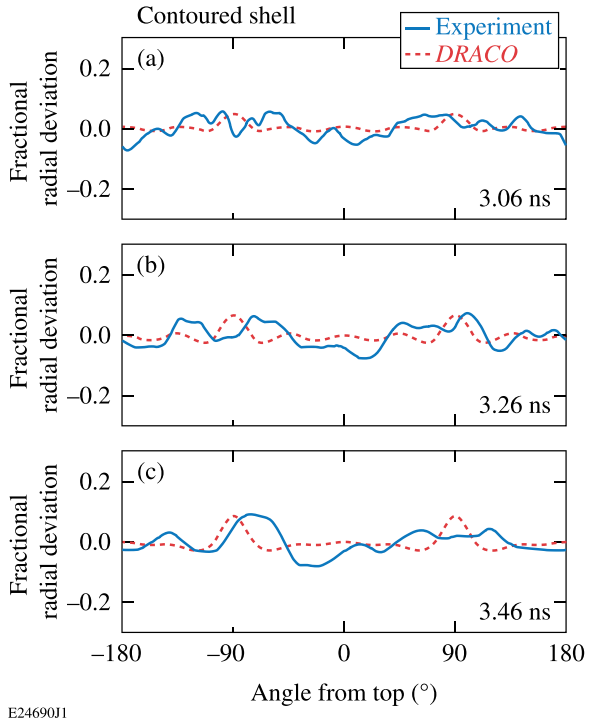

FIG. 9. Comparison of radiograph peak absorption shape with *DRACO* simulated shapes for the polar-driven contoured-shell implosion shown in Fig. 6.

modes $\mathscr{L}=2$ and $\mathscr{L}=4$ modes (i.e., a_2 and a_4) are shown as combined results from three spherical shells [Fig. 12(a)] and three contoured shells [Fig. 12(b)]. The spherical shells develop a significant negative a_2 ($\sim -20\%$) late in time indicative of an oblate shape and a_4 is significant and positive ($\sim +15\%$). The contoured-shell targets obtain a more nearly spherical shape with a_2 and a_4 being $\lesssim 5\%$ in amplitude for all times measured. The amplitudes determined from the simulations are close to those observed. For the spherical shells, both the sign and magnitude of a_2 from the simulation match the observations, whereas the magnitude of a_4 is slightly overpredicted compared to observations. This may indicate a difference in the actual and predicted distribution of material in the plasma at that time. Nevertheless, the contoured-shell targets obtain the most-symmetric shape in

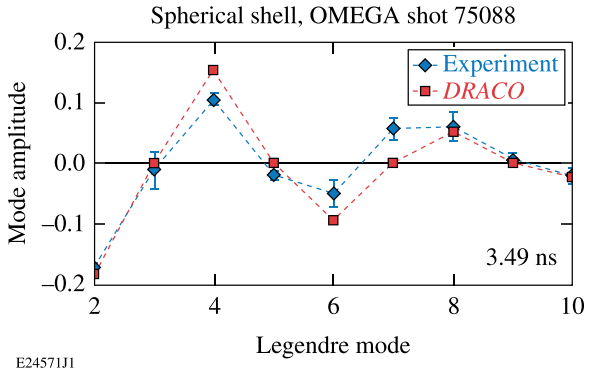

FIG. 10. Legendre-mode amplitudes (normalized to the average radius) determined from the radiograph peak amplitudes for the polar-driven spherical-shell implosion shown in Fig. 7(c) compared to those determined from the *DRACO* simulated radiograph.

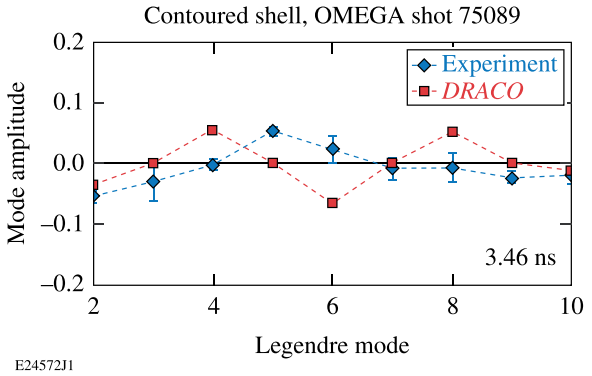

FIG. 11. Legendre-mode amplitudes (normalized to the average radius) determined from the radiograph peak amplitudes for the polar-driven contoured-shell implosion shown in Fig. 8(c) compared to those determined from the *DRACO* simulated radiograph.

both experiment and simulation with significantly reduced a_2 and a_4 amplitudes.

The D–D fusion neutron yields from the polar-driven, contoured-shell and spherical-shell implosions as a function of the mass-averaged shell thickness (equal to the shell thickness for spherical shells) are shown in Fig. 13. The yields shown are for both contoured and spherical shells for the beam-pointing case (0, 120, 140). Additional beam-pointing cases of (90, 120, 120), (90, 133, 133), and (90, 150, 150) were attempted with spherical shells in the course of experiments taken with identical laser conditions. Labeled as "PDD spherical (all other)," there is no significant difference in yield to the polar-driven spherical shells taken at pointing (0, 120, 140). Also shown are neutron yields for spherical shells imploded with 60-beam symmetric illumination, again with approximately the same total energy on target (~14 kJ). Not surprisingly, the symmetrically driven spherical shells produced the highest yields. In this case, all the beams were aimed at the target center, maximizing the coupling of energy to the target. For the PDD implosions, those with contoured shells produced yields that were higher than all of the polar-driven spherical shells by more than a factor of ~2 and were ~70% of the yields obtained by the symmetrically driven shells.

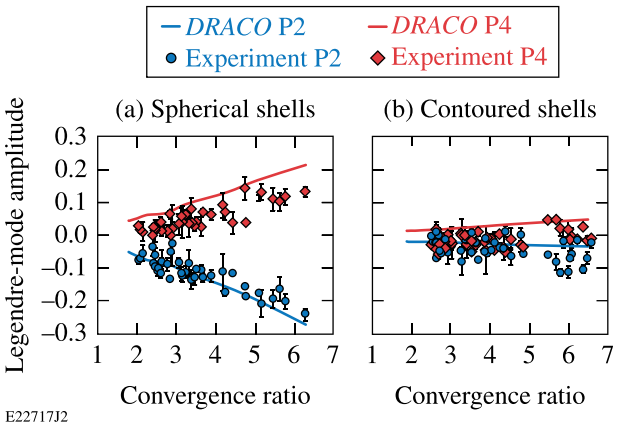

FIG. 12. Comparison of the radiograph measured and simulated $\lambda = 2$ and $\lambda = 4$ mode perturbations of polar-driven (a) spherical shells and (b) contoured shells. In both cases, a single *DRACO* simulation is compared to values determined from three nearly identical implosions.

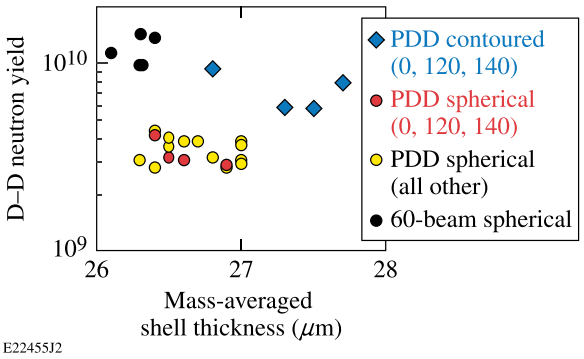

FIG. 13. Neutron yields from polar-driven spherical shells, polar-driven contoured shells, and symmetrically driven spherical shells. All were imploded with ~14 kJ of UV laser light, using a triple picket pulse shape.

That the increased yield of polar-driven contoured shells relative to polar-driven spherical shells is generated by an increased compression of the core and not by an average velocity change is further confirmed by comparing the D–D fusion neutron production rates measured by the neutron temporal diagnostic (NTD)[26] for a polar-driven spherical shell, a polar-driven contoured shell, and a spherically driven spherical shell (Fig. 14). Within the accuracy of measurements, core stagnation times are the same, whereas the polar-driven contoured shell achieves a large increase in yield relative to the polar-driven spherical shell, approaching that of the spherically driven spherical shell.

The areal densities of these implosions were inferred from measurements of the energy loss of protons resulting from secondary reactions in the D_2 fuel.[27] Two filtered CR39 packs were used per shot for one spherical-shell and two contoured-shell implosions. The average inferred areal densities are plotted in Fig. 15 compared to *DRACO* simulated values for two contoured-shell implosions and one spherical shell implosion at the beam-pointing case (0, 120, 140). For comparison, a previously obtained result also performed with the triple-picket pulse shape used in this work is also shown in Fig. 15.[28] The previous triple-picket pulse shape

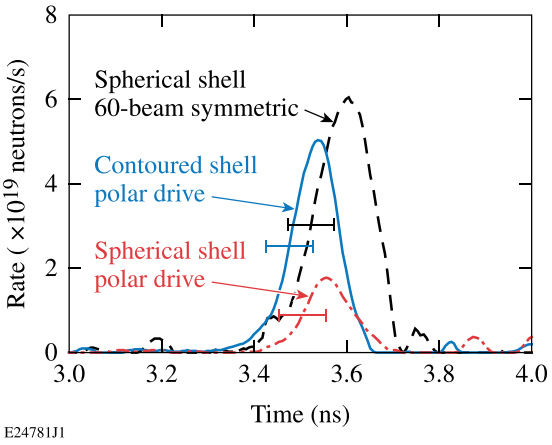

FIG. 14. Example fusion neutron-production rates measured by the NTD for a polar-driven spherical shell, a polar-driven contoured shell, and a symmetrically driven spherical shell. In each case, the horizontal error bar indicates the uncertainty in the absolute times of the measurements (50 ps). All were imploded with ~14 kJ of UV laser light, using a triple picket pulse shape.

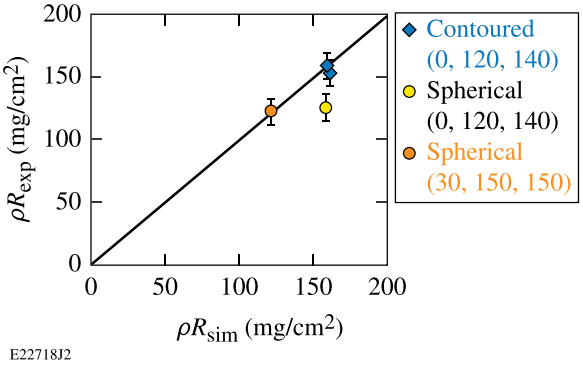

FIG. 15. Measured areal densities for polar-driven implosions with the beam-pointing case (0, 120, 140) for polar-driven contoured shells and polar-driven spherical shells. Also included is a case of a spherical shell for beam-pointing case (30, 150, 150). All were imploded with ~14 kJ of UV laser light, using a triple picket pulse shape.

implosion was performed using the beam-pointing case (30, 150, 150). The areal densities from the contoured shells exceed those obtained from the spherical shell in part because of the more-symmetric implosion and in part because of the increased fusion yield that produces secondary protons that sample the areal density later in the implosion when higher compression occurs.[28]

IV. CONCLUSIONS

As demonstrated by these experiments, shaping the target shell can increase the low-mode symmetry over beam repointing alone with a concomitant increase in the fusion yield and measured areal density. Given the need to control the shape of PDD implosions on the NIF, these results indicate that further research into methods to shape the DT encapsulating shell and or the DT layer itself should be undertaken. These experiments were performed at an intensity ($\sim 4 \times 10^{14}$ W/cm^2), where the loss of drive near the equator caused by CBET is expected to be of minimal effect. Fortunately, the method of compensating for reduced drive at the equator of the polar-driven shell by the reducing the shell thickness at the equator is not likely to be affected by the presence or lack of CBET. Rather, the shell-thickness profile can be chosen to match the drive conditions, taking into account the specific loss mechanisms such as CBET. Indirectly driven implosions may also benefit from using a contoured-shell target, emphasizing the importance of this method.

ACKNOWLEDGMENTS

This material is based upon work supported by the Department of Energy National Nuclear Security Administration under Award No. DE-NA0001944, the University of Rochester, and the New York State Energy Research and Development Authority. The support of DOE does not constitute an endorsement by DOE of the views expressed in this article.

[1]S. Skupsky, J. A. Marozas, R. S. Craxton, R. Betti, T. J. B. Collins, J. A. Delettrez, V. N. Goncharov, P. W. McKenty, P. B. Radha, T. R. Boehly, J. P. Knauer, F. J. Marshall, D. R. Harding, J. D. Kilkenny, D. D. Meyerhofer, T. C. Sangster, and R. L. McCrory, Phys. Plasmas **11**, 2763 (2004).
[2]G. H. Miller, E. I. Moses, and C. R. Wuest, Opt. Eng. **43**, 2841 (2004).
[3]T. R. Boehly, D. L. Brown, R. S. Craxton, R. L. Keck, J. P. Knauer, J. H. Kelly, T. J. Kessler, S. A. Kumpan, S. J. Loucks, S. A. Letzring, F. J. Marshall, R. L. McCrory, S. F. B. Morse, W. Seka, J. M. Soures, and C. P. Verdon, Opt. Commun. **133**, 495 (1997).
[4]R. S. Craxton, F. J. Marshall, M. J. Bonino, R. Epstein, P. W. McKenty, S. Skupsky, J. A. Delettrez, I. V. Igumenshchev, D. W. Jacobs-Perkins, J. P. Knauer, J. A. Marozas, P. B. Radha, and W. Seka, Phys. Plasmas **12**, 056304 (2005).
[5]F. J. Marshall, R. S. Craxton, M. J. Bonino, R. Epstein, V. Yu. Glebov, D. Jacobs-Perkins, J. P. Knauer, J. A. Marozas, P. W. McKenty, S. G. Noyes, P. B. Radha, W. Seka, S. Skupsky, and V. A. Smalyuk, J. Phys. IV France **133**, 153 (2006).
[6]F. J. Marshall, P. W. McKenty, J. A. Delettrez, R. Epstein, J. P. Knauer, V. A. Smalyuk, J. A. Frenje, C. K. Li, R. D. Petrasso, F. H. Séguin, and R. C. Mancini, Phys. Rev. Lett. **102**, 185004 (2009).
[7]P. B. Radha, J. A. Marozas, F. J. Marshall, A. Shvydky, T. J. B. Collins, V. N. Goncharov, R. L. McCrory, P. W. McKenty, D. D. Meyerhofer, T. C. Sangster, and S. Skupsky, Phys. Plasmas **19**, 082704 (2012).
[8]J. A. Cobble, T. J. Murphy, M. J. Schmitt, P. A. Bradley, N. S. Krasheninnikova, K. A. Obrey, S. C. Hsu, I. L. Tregillis, G. R. Magelssen, F. J. Wysocki, and S. H. Batha, Phys. Plasmas **19**, 122713 (2012).
[9]N. S. Krasheninnikova, J. A. Cobble, T. J. Murphy, I. L. Tregillis, P. A. Bradley, P. Hakel, S. C. Hsu, G. A. Kyrala, K. A. Obrey, M. J. Schmitt, J. A. Baumgaertel, and S. H. Batha, Phys. Plasmas **21**, 042703 (2014).
[10]J. A. Marozas, F. J. Marshall, R. S. Craxton, I. V. Igumenshchev, S. Skupsky, M. J. Bonino, T. J. B. Collins, R. Epstein, V. Yu. Glebov, D. Jacobs-Perkins, J. P. Knauer, R. L. McCrory, P. W. McKenty, D. D. Meyerhofer, S. G. Noyes, P. B. Radha, T. C. Sangster, W. Seka, and V. A. Smalyuk, Phys. Plasmas **13**, 056311 (2006).
[11]T. J. B. Collins, J. A. Marozas, K. S. Anderson, R. Betti, R. S. Craxton, J. A. Delettrez, V. N. Goncharov, D. R. Harding, F. J. Marshall, R. L. McCrory, D. D. Meyerhofer, P. W. McKenty, P. B. Radha, A. Shvydky, S. Skupsky, and J. D. Zuegel, Phys. Plasmas **19**, 056308 (2012).
[12]M. Hohenberger, P. B. Radha, J. F. Myatt, S. LePape, J. A. Marozas, F. J. Marshall, D. T. Michel, S. P. Regan, W. Seka, A. Shvydky, T. C. Sangster, J. W. Bates, R. Betti, T. R. Boehly, M. J. Bonino, D. T. Casey, T. J. B. Collins, R. S. Craxton, J. A. Delettrez, D. H. Edgell, R. Epstein, G. Fiksel, P. Fitzsimmons, J. A. Frenje, D. H. Froula, V. N. Goncharov, D. R. Harding, D. H. Kalantar, M. Karasik, T. J. Kessler, J. D. Kilkenny, J. P. Knauer, C. Kurz, M. Lafon, K. N. LaFortune, B. J. MacGowan, A. J. Mackinnon, A. G. MacPhee, R. L. McCrory, P. W. McKenty, J. F. Meeker, D. D. Meyerhofer, S. R. Nagel, A. Nikroo, S. Obenschain, R. D. Petrasso, J. E. Ralph, H. G. Rinderknecht, M. J. Rosenberg, A. J. Schmitt, R. J. Wallace, J. Weaver, C. Widmayer, S. Skupsky, A. A. Solodov, C. Stoeckl, B. Yaakobi, and J. D. Zuegel, Phys. Plasmas **22**, 056308 (2015).
[13]T. J. Murphy, N. S. Krasheninnikova, G. A. Kyrala, P. A. Bradley, J. A. Baumgaertel, J. A. Cobble, P. Hakel, S. C. Hsu, J. L. Kline, D. S. Montgomery, K. A. D. Obrey, R. C. Shah, I. L. Tregillis, M. J. Schmitt, R. J. Kanzleiter, S. H. Batha, R. J. Wallace, S. D. Bhandarkar, P. Fitzsimmons, M. L. Hoppe, A. Nikroo, M. Hohenberger, P. W. McKenty, H. G. Rinderknecht, M. J. Rosenberg, and R. D. Petrasso, Phys. Plasmas **22**, 092707 (2015).
[14]W. L. Kruer, S. C. Wilks, B. B. Afeyan, and R. K. Kirkwood, Phys. Plasmas **3**, 382 (1996).
[15]I. V. Igumenshchev, D. H. Edgell, V. N. Goncharov, J. A. Delettrez, A. V. Maximov, J. F. Myatt, W. Seka, A. Shvydky, S. Skupsky, and C. Stoeckl, Phys. Plasmas **17**, 122708 (2010).
[16]F. H. Séguin, C. K. Li, J. L. DeCiantis, J. Frenje, J. R. Rygg, R. D. Petrasso, F. J. Marshall, V. Smalyuk, V. Yu. Glebov, J. Knauer, T. C. Sangster, J. D. Kilkenny, and A. Nikroo, "Effects of fuel-capsule shimming and drive asymmetry on inertial-confinement-fusion symmetry and yield," Phys. Plasmas (to be published).
[17]J. D. Lindl, P. Amendt, R. L. Berger, S. G. Glendinning, S. H. Glenzer, S. W. Haan, R. L. Kauffman, O. L. Landen, and L. J. Suter, Phys. Plasmas **11**, 339 (2004).
[18]J. Delettrez, R. Epstein, M. C. Richardson, P. A. Jaanimagi, and B. L. Henke, Phys. Rev. A **36**, 3926 (1987).
[19]General Atomics, San Diego, CA 92121-1122.
[20]S. Skupsky, R. W. Short, T. Kessler, R. S. Craxton, S. Letzring, and J. M. Soures, J. Appl. Phys. **66**, 3456 (1989).

[21]T. R. Boehly, V. A. Smalyuk, D. D. Meyerhofer, J. P. Knauer, D. K. Bradley, R. S. Craxton, M. J. Guardalben, S. Skupsky, and T. J. Kessler, J. Appl. Phys. **85**, 3444 (1999).
[22]R. A. Forties and F. J. Marshall, Rev. Sci. Instrum. **76**, 073505 (2005).
[23]P. B. Radha, V. N. Goncharov, T. J. B. Collins, J. A. Delettrez, Y. Elbaz, V. Yu. Glebov, R. L. Keck, D. E. Keller, J. P. Knauer, J. A. Marozas, F. J. Marshall, P. W. McKenty, D. D. Meyerhofer, S. P. Regan, T. C. Sangster, D. Shvarts, S. Skupsky, Y. Srebro, R. P. J. Town, and C. Stoeckl, Phys. Plasmas **12**, 032702 (2005).
[24]D. K. Bradley, P. M. Bell, O. L. Landen, J. D. Kilkenny, and J. Oertel, Rev. Sci. Instrum. **66**, 716 (1995).
[25]J. J. MacFarlane, I. E. Golovkin, P. Wang, P. R. Woodruff, and N. A. Pereyra, High Energy Density Phys. **3**, 181 (2007).
[26]R. A. Lerche, D. W. Phillion, and G. L. Tietbohl, Rev. Sci. Instrum. **66**, 933 (1995).
[27]F. H. Séguin, C. K. Li, J. A. Frenje, D. G. Hicks, K. M. Green, S. Kurebayashi, R. D. Petrasso, J. M. Soures, D. D. Meyerhofer, V. Yu. Glebov, P. B. Radha, C. Stoeckl, S. Roberts, C. Sorce, T. C. Sangster, M. D. Cable, K. Fletcher, and S. Padalino, Phys. Plasmas **9**, 2725 (2002).
[28]P. B. Radha, F. J. Marshall, J. A. Marozas, A. Shvydky, I. Gabalski, T. R. Boehly, T. J. B. Collins, R. S. Craxton, D. H. Edgell, R. Epstein, J. A. Frenje, D. H. Froula, V. N. Goncharov, M. Hohenberger, R. L. McCrory, P. W. McKenty, D. D. Meyerhofer, R. D. Petrasso, T. C. Sangster, and S. Skupsky, Phys. Plasmas **20**, 056306 (2013).